International Journal of Microwave and Wireless Technologies

cambridge.org/mrf

An effective parametric approach for patient-specific head model generation in quantitative microwave imaging

Darko Ninković[1], Anja Kovačević[1], Branko M. Kolundzija[1,2], Rosa Scapaticci[3], Lorenzo Crocco[3] and Marija Nikolić Stevanović[1]

[1]School of Electrical Engineering, University of Belgrade, Belgrade, Serbia; [2]WIPL-D doo, Belgrade, Serbia and [3]Institute for Electromagnetic Sensing of Environment, National Research Council of Italy, Napoli, Italy

Research Paper

Cite this article: Ninković D, Kovačević A, Kolundzija BM, Scapaticci R, Crocco L, Nikolić Stevanović M (2026) An effective parametric approach for patient-specific head model generation in quantitative microwave imaging. *International Journal of Microwave and Wireless Technologies* **18**(3), 498–507. https://doi.org/10.1017/S175907872610333X

Received: 31 October 2025
Revised: 1 May 2026
Accepted: 8 May 2026
First published online: 28 May 2026

Corresponding author: Darko Ninković;
Email: darko@etf.bg.ac.rs

Abstract

Medical microwave imaging (MMWI) is emerging as a promising noninvasive diagnostic modality, offering a safe, portable, and cost-effective alternative to conventional imaging methods. Despite its potential, MMWI poses significant challenges due to the ill-posed and nonlinear nature of the underlying inverse scattering problem. Two main strategies are typically adopted: qualitative imaging, which yields rapid but approximate reconstructions, and quantitative imaging, which aims to recover the full permittivity distribution of tissues. Both approaches substantially benefit from accurate patient-specific background models that enhance reliability and reduce computational complexity. Building upon preliminary results presented at EuCAP 2025, this work advances the development of patient-specific head models for quantitative brain imaging. The study employs anatomically conformal basis functions and extends the model to include cerebrospinal fluid, which represents a strong scatterer with markedly distinct dielectric properties. The proposed framework improves reconstruction accuracy and convergence efficiency, thereby contributing to the advancement of quantitative MMWI toward practical clinical applications.

Introduction

Medical microwave imaging (MMWI) has gained increasing attention as a noninvasive diagnostic technique due to its low cost and use of nonionizing radiation [1–7]. Conventional medical imaging modalities, including magnetic resonance imaging (MRI), computed tomography (CT), and positron emission tomography (PET), remain the gold standard for clinical diagnostics, offering high-resolution images. However, their widespread use is limited by high operational costs, sizable equipment, and, in the case of CT and PET, exposure to potentially harmful ionizing radiation. In contrast, MMWI provides a portable, safe, and cost-effective alternative that mitigates many drawbacks of MRI and CT, albeit with reduced spatial resolution. Among its various potential applications, brain imaging (particularly for stroke or tumor detection and follow-up) has emerged as one of the most promising areas for MMWI development [2], highlighting its potential for rapid bedside diagnostic assessments.

Implementing MMWI entails solving an ill-posed and highly nonlinear inverse scattering problem [4], which poses a significant computational challenge. To address this, two main strategies have been proposed in the literature. The first strategy involves formulating a linearized version of the inverse problem to reconstruct qualitative, real-time images of the examined region. This approach is effective primarily for detecting small anomalies, under the assumption that prior patient-specific information about healthy tissues is available. In the absence of such information, however, qualitative MMWI reconstructions tend to be unreliable.

The second strategy, known as quantitative imaging, aims to reconstruct the complex permittivity distribution within the whole region of interest, including that of the stroke or tumor. Since biological tissues exhibit distinct permittivity values, this approach produces scan-like images reflecting tissue distribution. Quantitative imaging involves solving the full nonlinear inverse scattering problem, typically through iterative techniques such as inexact Newton methods [8, 9] or distorted Born iterative methods (DBIMs) [10–14]. However, these methods are often computationally prohibitive due to their iterative nature. More critically, they are susceptible to false solutions, estimates that satisfy the measured data but deviate from the true permittivity distribution. Both excessive computational cost and the risk of false

© The Author(s), 2026. Published by Cambridge University Press in association with The European Microwave Association. This is an Open Access article, distributed under the terms of the Creative Commons Attribution licence (http://creativecommons.org/licenses/by/4.0), which permits unrestricted re-use, distribution and reproduction, provided the original article is properly cited.

reconstructions can be mitigated by employing patient-specific background models as initial estimates in the optimization process.

Based on the above discussion, having an appropriate patient-specific model is crucial for improving performance in both qualitative and quantitative inverse scattering approaches. In qualitative imaging, the model must be sufficiently accurate to enable rapid detection of subtle tissue variations, such as tumor growth or disease progression. In quantitative imaging, where the aim is to capture finer tissue changes, the model serves as a reliable initialization that guides the optimization process toward the true solution, accelerates convergence, and significantly reduces the number of required iterations, making these algorithms more practical for real-time diagnostic applications.

The concept of a patient-specific background model was first introduced at the EuCAP 2025 Conference and published in its proceedings [15], where preliminary results were reported. In that work, initial head images were reconstructed using a linear inverse-scattering model based on the Born approximation and regularized with polynomial basis functions representing the contrast. These images were subsequently segmented and converted into a four-domain phantom, with the permittivities of each domain estimated using a suitably formulated DBIM approach. The techniques for phantom generation from MMWI images are further refined and extended in Ninković et al. [16], along with a stroke detection analysis that could benefit from the patient-specific background model.

In this work, we introduce several key improvements over Nincović et al. [15, 16]. The primary advancement lies in the use of conformal basis functions, rather than polynomial basis functions, to model the unknown contrast. Specifically, a combination of low-order spherical harmonics is employed to capture angular deviations from the outer head geometry, while radial pulse functions are used to represent the rapidly varying permittivity along the radial direction. This formulation enables a more accurate delineation of tissue boundaries, improves reconstruction accuracy, and reduces the number of required basis functions, thereby alleviating the ill-posedness of the problem.

In addition, a more realistic and complex phantom is considered compared to Ninković et al. 15, 16], incorporating an additional tissue layer corresponding to cerebrospinal fluid (CSF). Finally, the robustness of the proposed method under practical conditions is evaluated by introducing noise into the scattering parameters across a range of signal-to-noise ratio (SNR) levels.

Thus, the main outcome of this work is an improved four-domain phantom, together with corresponding estimates of tissue permittivities. The proposed phantom can serve as a fast, patient-specific approximation of a healthy head and can be integrated as an initial modeling step within a clinical workflow, enabling rapid stroke detection even when only limited prior information, such as the outer head shape, is available. This capability is particularly valuable in time-critical scenarios, when conventional imaging modalities may not be readily accessible.

The remainder of this paper is organized as follows: The "Parametric modeling of the permittivity distribution" section introduces the selected parametric model for representing the permittivity distribution. The "MMWI scenario" section details the considered MMWI scenario. In the "Distorted Born iterative method" section, the applied formulation of DBIM is outlined. The obtained results for the numerical example are presented in the "Numerical example" section. Finally, the "Conclusion" section provides the concluding remarks.

Parametric modeling of the permittivity distribution

To mitigate the ill-posedness of the inverse problem, it is advantageous to represent the unknown permittivity distribution using suitable basis functions, thereby reducing the dimensionality of the solution space. In the upper head region, head tissues are approximately conformal to the overall head shape. Therefore, it is reasonable to employ basis functions that follow this outer geometry while still accommodating variations, which can be effectively modeled using low-order spherical harmonics. Each point on the head surface can be represented as

$$R_s(\theta,\varphi) \approx \sum_{l=0}^{L}\sum_{m=-l}^{l} a_{lm} Y_l^m(\theta,\varphi), \tag{1}$$

where $Y_l^m(\theta,\varphi)$ is the spherical harmonic of the degree l and order m, L is the maximal degree of spherical harmonics, and a_{lm} are the expansion coefficients. Similarly, the permittivity distribution, represented as a three-dimensional (3D) function in the spherical coordinate system, $\varepsilon(r,\theta,\varphi)$, can be approximated by a series of orthogonal basis functions formed as the product of radial functions – which model radial dependence – and spherical harmonics, which capture angular dependence. This expansion takes the form:

$$\varepsilon(r,\theta,\varphi) \approx \sum_{n=1}^{N}\sum_{l=0}^{L}\sum_{m=-l}^{l} c_{nlm} p_n(\hat{r}) Y_l^m(\theta,\varphi), \tag{2}$$

where c_{nlm} are the corresponding expansion coefficients, $\hat{r}$ is the normalized radial coordinate

$$\hat{r}(r,\theta,\varphi) = \frac{R_s(\theta,\varphi) - r}{R_s(\theta,\varphi)}, \tag{3}$$

(i.e., the normalized radial distance from the head surface), $p_n(\hat{r})$ are the radial pulse or indicator basis functions, $n = 1,\ldots,N$, defined as

$$p_n(\hat{r}) = \begin{cases} 1, & \text{if } r' \in [(n-1)/N,\ n/N) \\ 0, & \text{otherwise} \end{cases}. \tag{4}$$

In the numerical implementation, the space is uniformly divided into K voxels, with each voxel having the constant permittivity, ε_k, $k = 1,\ldots,K$. In matrix form, this can be written as

$$\boldsymbol{\varepsilon} = \mathbf{H}\mathbf{c}, \tag{5}$$

where $\boldsymbol{\varepsilon}$ is the vector of unknown permittivities

$$\boldsymbol{\varepsilon} = \begin{bmatrix} \varepsilon_1 & \ldots & \varepsilon_K \end{bmatrix}^{\mathrm{T}}, \tag{6}$$

$\mathbf{c}$ is the vector of the unknown coefficients

$$\mathbf{c} = \begin{bmatrix} c_1 & \ldots & c_Q \end{bmatrix}^{\mathrm{T}}, \tag{7}$$

and Q is the total number of coefficients $Q = N(L+1)^2$. In (7), we used simplified notation $c_j = c_{nlm}$, where j is a single index corresponding to a triplet (n, l, m), $j = 1, \ldots, Q$. Furthermore, $\mathbf{H}$ is the transformation matrix whose elements are calculated as

$$\mathbf{H}(k,j) = p_n(\hat{r}_k)\, Y_l^m(\theta_k,\varphi_k),\ k = 1,\ \ldots,\ K,\ j = 1,\ \ldots,\ Q, \tag{8}$$

where (r_k,θ_k,φ_k) are the spherical coordinates of the kth voxel and $\hat{r}_k = \frac{R_s(\theta_k,\varphi_k) - r_k}{R_s(\theta_k,\varphi_k)}$.

https://doi.org/10.1017/S175907872610333X Published online by Cambridge University Press

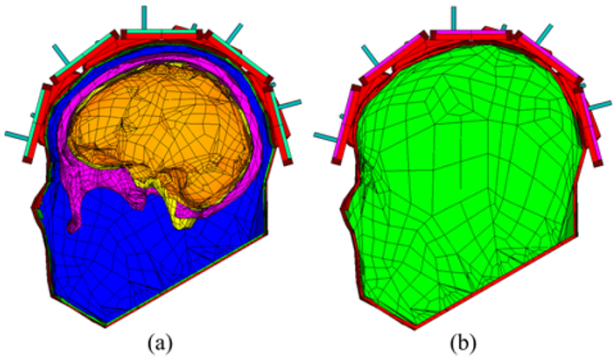


Figure 1. (a) Brain imaging scenario. (b) Initial background model.

MMWI scenario

Figure 1 (a) illustrates an MMWI scenario, consisting of an array of antennas in close contact with the head. In the considered example, the head model comprises six homogeneous tissues. The assumed initial background model, shown in Fig. 1(b), represents a homogeneous head with a permittivity equal to that of brain tissue and includes a thin layer corresponding to the skin. The underlying physical model is the scattering equation, which, under the Born approximation, is given by [17, 18]:

$$\Delta_{S_{ij}} \approx -\frac{\mathrm{j}\omega}{2a_i a_j}\int_{v'}\Delta\varepsilon(\boldsymbol{r}')\boldsymbol{E}_{\mathrm{i}}^{i}(\boldsymbol{r}')\cdot\boldsymbol{E}_{\mathrm{i}}^{j}(\boldsymbol{r}')\mathrm{d}v',\, i,j=1,\ldots,M, \tag{9a}$$

$$\Delta S_{i,j} = S_{i,j} - S_{i,j}^{0}, \Delta\varepsilon_k = \varepsilon_k - \varepsilon_{k,\mathrm{b}}, \tag{9b}$$

where s_{ij} and s_{ij}^0 are the transmission coefficients between the ith and jth antennas, computed or measured for the actual system and assumed background, respectively, ε is the unknown head permittivity,ε_{b} is the known permittivity of the background model, $\Delta\varepsilon$ is the permittivity difference, $\mathbf{r}'$is the position vector of a point inside the head, $\mathbf{E}_{\mathrm{i}}^{i(j)}$ is the electric field vector computed in the background model when the $i(j)$th antenna is transmitting, $a_{i(j)}$ is the complex amplitude of the incident power wave at the $i(j)$th port, M is the size of the array, v' is the known volume occupied by the head, and ω is the angular frequency.

In the discrete case, (9) becomes

$$\Delta_{S_{ij}} \approx -\frac{\mathrm{j}\omega\Delta v}{2a_i a_j}\sum_{K=1}^{K}\Delta\varepsilon_k\boldsymbol{E}_{\mathrm{i}}^{i}(\boldsymbol{t}_k)\cdot\boldsymbol{E}_{i}^{j}(\boldsymbol{t}_k),\; i,j=1,\ldots,M \tag{10a}$$

$$\Delta\varepsilon_k = \varepsilon_k - \varepsilon_{k,\mathrm{b}},\; k=1,\ldots,K, \tag{10b}$$

where $\mathbf{t}_k$ is the position vector of the center of the kth voxel, and ε_k, and $\varepsilon_{k,\mathrm{b}}$ are the constant permittivities of the kth voxel in the actual head and background model, respectively, $\Delta\varepsilon_k$ is their difference, Δv is the volume of each voxel, and K is the total number of voxels into which the occupied volume is divided. In matrix form, (10) becomes

$$\Delta\mathbf{s} = \mathbf{L}\Delta\boldsymbol{\varepsilon}, \tag{11}$$

with

$$\Delta\mathbf{s} = \begin{bmatrix}\Delta s_{1,1} & \Delta s_{1,2} & \cdots & \Delta s_{M,M}\end{bmatrix}^{\mathrm{T}}, \tag{12a}$$

$$\mathbf{L} = -\frac{\mathrm{j}\omega\Delta v}{2}\cdot\begin{bmatrix}\frac{\mathbf{E}_{\mathrm{i}}^{1}(\mathbf{t}_1)\cdot\mathbf{E}_{\mathrm{i}}^{1}(\mathbf{t}_1)}{a_1a_1} & \cdots & \frac{\mathbf{E}_{\mathrm{i}}^{1}(\mathbf{t}_L)\cdot\mathbf{E}_{\mathrm{i}}^{1}(\mathbf{t}_L)}{a_1a_1}\\ \frac{\mathbf{E}_{\mathrm{i}}^{1}(\mathbf{t}_1)\cdot\mathbf{E}_{\mathrm{i}}^{2}(\mathbf{t}_1)}{a_1a_2} & \vdots & \frac{\mathbf{E}_{\mathrm{i}}^{1}(\mathbf{t}_L)\cdot\mathbf{E}_{\mathrm{i}}^{2}(\mathbf{t}_L)}{a_1a_2}\\ \vdots & \vdots & \vdots\\ \frac{\mathbf{E}_{\mathrm{i}}^{M}(\mathbf{t}_1)\cdot\mathbf{E}_{\mathrm{i}}^{M}(\mathbf{t}_1)}{a_Ma_M} & \cdots & \frac{\mathbf{E}_{\mathrm{i}}^{M}(\mathbf{t}_L)\cdot\mathbf{E}_{\mathrm{i}}^{M}(\mathbf{t}_L)}{a_Ma_M}\end{bmatrix}, \tag{12b}$$

$$\Delta\boldsymbol{\varepsilon} = \begin{bmatrix}\Delta\varepsilon_1 & \ldots & \Delta\varepsilon_L\end{bmatrix}^{\mathrm{T}}. \tag{12c}$$

We express the permittivity difference vector (12c) using the adopted basis functions (5) as

$$\Delta\boldsymbol{\varepsilon} = \mathbf{H}\boldsymbol{c}. \tag{13}$$

When (13) is inserted into (11), we obtain the final system of equations relating the measurements and the polynomial coefficients

$$\boldsymbol{\Delta s} = \mathbf{A}\boldsymbol{c}, \tag{14}$$

where $\mathbf{A} = \mathbf{LH}$. To solve (14), the Tikhonov regularization is adopted. The corresponding cost function is

$$J = \|\boldsymbol{\Delta s} - \mathbf{A}\boldsymbol{c}\|_2^2 + \lambda\|\mathbf{H}\boldsymbol{c}\|_2^2 \tag{15}$$

where λ is regularization coefficient. The solution of (15) is

$$\tilde{\boldsymbol{c}} = \left(\mathbf{A}^{\mathrm{H}}\mathbf{A} + \lambda\mathbf{H}^{\mathrm{H}}\mathbf{H}\right)^{-1}\mathbf{A}^{\mathrm{H}}\boldsymbol{\Delta s} \tag{16}$$

and the estimated permittivity vector is

$$\tilde{\boldsymbol{\varepsilon}} = \mathbf{H}\tilde{\boldsymbol{c}} + \boldsymbol{\varepsilon}_{\mathrm{b}} \tag{17}$$

where

$$\boldsymbol{\varepsilon}_{\mathrm{b}} = \begin{bmatrix}\varepsilon_{1,\mathrm{b}} & \ldots & \varepsilon_{K,\mathrm{b}}\end{bmatrix}^{\mathrm{T}}, \tag{18}$$

$\boldsymbol{\varepsilon}_{\mathrm{b}}$ is the background permittivity vector. Based on the approximate solution (17), we extract information about the skull by assuming that all voxels with intensity below a chosen threshold correspond to the skull, due to its low permittivity. Once the skull is identified, its interior is assumed to represent the brain. The model is then completed by adding a thin surface layer, conformal to the outer head shape. As a result, a parametric head model comprising four homogenous tissues is obtained.

Distorted Born iterative method

Once the parametric head model is obtained, we calculate the complex permittivities of its domains using the DBIM.

The DBIM has been widely employed in MMWI, with notable applications such as the following. A calibrated, frequency-division DBIM-based two-dimensional (2D) microwave tomography algorithm for head imaging was validated on head phantoms and healthy volunteers [10]. A 3D adaptive clustering DBIM approach for stroke detection was evaluated using a head scanner system and head phantoms, under the assumption that the number of tissues in the imaged domain and their approximate electromagnetic properties are known [11]. A brain stroke detection algorithm using the DBIM with two-step iterative shrinkage thresholding (DBIM-TwIST) was experimentally validated on a 2D head phantom, encircled by a ring of antennas [12]. A resolution-enhanced DBIM with a region-of-interest limitation scheme for microwave breast imaging yielded promising results on 2D numerical models [13]. The extended Born iterative method, incorporating a localized nonlinear approximation, achieved fast convergence and robust anomaly detection in realistic 2D numerical models

https://doi.org/10.1017/S175907872610333X Published online by Cambridge University Press

of stroke and breast tumors [14]. Unlike previous approaches, we apply the DBIM using previously estimated tissue boundaries, reducing the number of unknowns to the number of tissues without requiring patient-specific a priori information.

General DBIM formulation

The DBIM solves (10) by iteratively updating the estimated values of the permittivities in the background model $\varepsilon_{k,b}$, and values of Δs_{ij} and $\mathbf{E}_i^{i(j)}$ corresponding to the estimates of the $\varepsilon_{k,\mathrm{b}}$, where the background model is obtained by the procedure described in the previous section. To start the DBIM algorithm, the permittivity values $\varepsilon_{1,\mathrm{b}}^{(1)},\ \varepsilon_{2,\mathrm{b}}^{(1)},\ \ldots,\varepsilon_{K,\mathrm{b}}^{(1)}$, must be initialized.

In the lth iteration, the linear system of equations (11) is

$$\Delta\mathbf{s}^{(l)} = \mathbf{L}^{(l)}\Delta\boldsymbol{\varepsilon}^{(l)}, \tag{19}$$

where $\Delta\mathbf{s}^{(l)}$, $\mathbf{L}^{(l)}$, and $\Delta\boldsymbol{\varepsilon}^{(l)}$ are values of matrices in the lth iteration.

The system (19) is solved using truncated singular value decomposition. The regularized solution is

$$\Delta\boldsymbol{\varepsilon}^{(l)} = \sum_{n=1}^{n_{\max}} \frac{1}{\sigma_n}\left(\mathbf{u}_n^{\mathrm{H}}\cdot\Delta\mathbf{s}^{(l)}\right)\mathbf{v}_n\,, \tag{20}$$

where $\mathbf{u}_n$, and $\mathbf{v}_n$ are the singular vectors of matrix $\mathbf{L}^{(l)}$, σ_n are the corresponding singular values, and $n_{\max}$ is the truncation index, calculated using condition $10\log_{10}\left(\frac{\sigma_{n_{\max}}}{\sigma_1}\right) < -20$ dB. The permittivity estimate in the next iteration is calculated as

$$\hat{\boldsymbol{\varepsilon}}^{(l+1)} = \hat{\boldsymbol{\varepsilon}}^{(l)} + \Delta\hat{\boldsymbol{\varepsilon}}^{(l)}. \tag{21}$$

The DBIM algorithm is stopped when the magnitude of each member of the vector $\Delta\boldsymbol{\varepsilon}^{(l)}$ is smaller than some predefined threshold (set to 0.01 in all experiments presented in this work) or when the maximum number of iterations is reached.

DBIM formulation with known domain boundaries

If the domain of interest can be partitioned into subdomains of homogeneous permittivity with known boundaries, the number of unknown parameters is reduced to the number of these subdomains. The corresponding measurement model can then be expressed as

$$\Delta\mathbf{s}^{(l)} = \mathbf{L}^{(l)}\mathbf{W}\,\Delta\boldsymbol{\varepsilon}^{(l)}, \tag{22}$$

where $\mathbf{W}$ is the transformational matrix of size $K \times S$, and S is the number of subdomains. The (k, j) element of $\mathbf{W}$ equals 1 if the kth voxel belongs to the jth domain and 0 otherwise. The unknown vector is, thus,

$$\Delta\boldsymbol{\varepsilon}^{(l)} = \left[\ \Delta\varepsilon_1^{(l)} \quad \Delta\varepsilon_2^{(l)} \quad \cdots \quad \Delta\varepsilon_S^{(l)}\ \right]^{\mathrm{T}}, \tag{23}$$

where $\Delta\varepsilon_j^{(l)}$ refers to the contrast of the jth domain in the lth iteration.

Numerical example

As a numerical example, a realistic head phantom shown in Fig. 1 (a) is considered. The phantom is based on the NEVA female anatomical model [19] and adapted for MMWI applications within the WIPL-D Pro simulation environment [20]. The phantom consists of six homogeneous tissue layers, as illustrated in Fig. 1(a), with their respective permittivity values listed in Table 1. We assume that the outer surface of the phantom is known and given by a triangular mesh in Fig. 2. In reality, geometrical information is needed only in the upper part of the head below the helmet. The measurement setup comprised a helmet equipped with 21 closely spaced trapezoidal patch antennas, each operating at 1 GHz and optimized for performance in the presence of the head model. Further details regarding the head phantom and the measurement system configuration are provided in Singh et al. [21].

Table 1. Complex permittivity of head tissues @ 1 GHz

Tissue	Complex permittivity
Skin	45.71–j15.84
Fat	11.29–j2.09
Soft tissue	45.66–j15.95
Skull	20.58–j6.54
CSF	68.44–j44.13
Brain	52.28 –j17.71

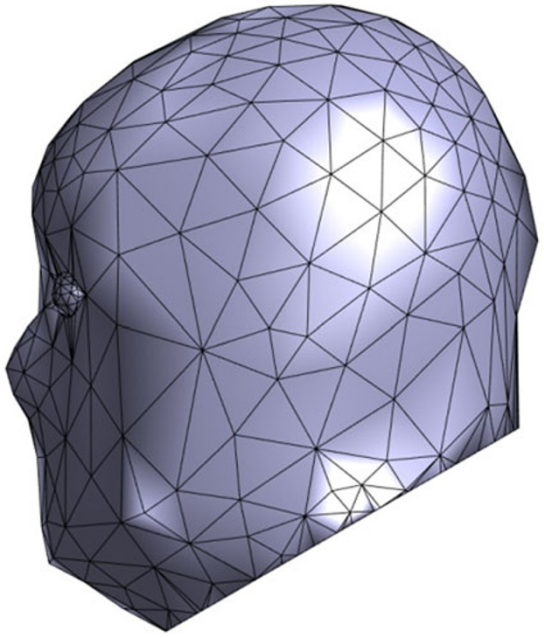


Figure 2. Triangular mesh of the skin layer of the phantom from Figure 1.

All results presented in this paper are generated using a desktop computer: Intel Core i7-9700 CPU @3 GHz, NVIDIA GeForce GTX 750 Ti GPU, with 32 GB of RAM under the Windows 10 operating system.

Parametric model creation

The first step involves extracting points on the head surface within a defined region of interest where the skull and overlying tissues are approximately conformal. These points are then used to construct a closed surface. Since the triangular mesh, shown in Fig. 2, is relatively rough, we first interpolate additional surface points and subsequently extract those located near the helmet, as illustrated in Fig. 3(a). To ensure geometric uniformity, the boundary points in each slice are then mapped onto a uniform angular grid

https://doi.org/10.1017/S175907872610333X Published online by Cambridge University Press

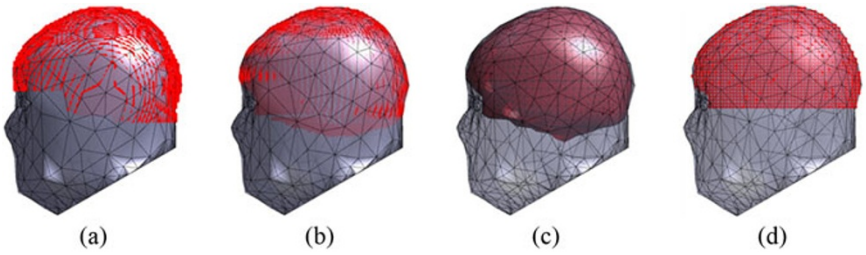


Figure 3. Computation of the boundary surface. (a) Portion of the head surface used for mapping, with corresponding surface points. (b) Extrapolated surface points arranged on a uniform polar grid in each horizontal cross-section. (c) Reconstructed boundary surface. (d) Final set of points used for imaging.

in polar coordinates, providing a consistent number of points per layer. Finally, to complete the closed surface, additional points are generated by shrinking the lowest layer and translating it downward, as shown in Fig. 3(b). The resulting extrapolated surface points serve as the matching points for the spherical approximation, the outcome of which is shown in Fig. 3 (c). In computing the spherical harmonic approximation, we assume that the *xy*-plane coincides with the layer where the head has the maximum perimeter. The expansion coefficients are used for calculating the normalized radius in (2).

For microwave imaging, we use a uniform 3D grid, within the defined closed surface and above $z_{\min} = -0.02$ m. This resulted in a total of 34,947 voxels of side length 4 mm, as shown in Fig. 2 (d). Lower regions were omitted due to insufficient field penetration, which limited their utility for reliable imaging.

Regarding permittivity expansion (2), along the radial direction, we set $N = 25$ pulses for radial variation, and $L = 3$ for the maximal order of the spherical harmonics expansion. The number of pulses is selected as a trade-off between spatial resolution and numerical stability. The order of the spherical harmonics is kept low to preserve the conformality of tissues, while still allowing a certain degree of flexibility.

As the assumed background model, the two-tissue head phantom presented in Fig. 1 (b) was used. The outer tissue mimicked skin and fat, and its permittivity was set to 28.50–j8.96, as the average value of the skin and fat permittivity values. The adopted thickness was 3.5 mm. The permittivity of the inner tissue was set to the value of the brain permittivity.

The results for selected cross-sections (out of 30, ordered from the lowest to the highest layer) are shown in Fig. 4. In each image pair, the right-hand image represents the reconstructed contrast (real part of the permittivity difference), while the left-hand image shows the true contrast, both relative to the adopted background model.

The influence of the number of pulses and the maximal spherical harmonics order was examined through a sensitivity analysis. The reconstruction results for different parameter choices are illustrated in Fig. 5. Specifically, increasing the number of pulses to $N = 30$ and the maximal spherical harmonics order to $L = 4$ leads to only minor variations in the reconstructed permittivity distribution. These results indicate that the proposed method is robust to moderate changes in the values of the parameters, while the selected values $N = 25$ and $L = 3$ provide a good balance between reconstruction accuracy and computational efficiency.

It should be noted that the total number of unknown coefficients in the proposed formulation is given by $N(L+1)^2$, which for $N = 25$ and $L = 3$ yields 400 unknowns. For comparison, in our previous work based on polynomial basis functions [15, 22], the number of unknowns was $(Q+1)^3 = 13^3 = 2197$, where Q denotes the maximum polynomial order. This substantial reduction in the number of unknown coefficients improves the conditioning of the inverse problem and contributes to the stability of the reconstruction, without compromising accuracy.

Furthermore, the robustness of the proposed method with respect to measurement noise was evaluated. To this end, additive white Gaussian noise (AWGN) was introduced to the scattering parameters of the original six-domain model.

In assessing acceptable noise levels, we considered that the signal-to-modeling-error power ratio for the initial two-layer background model is approximately 11 dB, indicating a significant modeling mismatch at the starting point. Additionally, in applications such as stroke diagnostics [23], the signal associated with pathological regions is typically 50–70 dB lower than the measured signal. Consequently, MWI systems operating with noise levels exceeding this range would not be suitable for reliable stroke detection.

Nevertheless, in our analysis, we considered SNR values as low as 10 dB to evaluate the robustness of the proposed approach. Figure 6 presents reconstructed head images for a selected cross-sectional slice located away from the surface. Results are shown for SNR values of 20 and 10 dB, alongside the corresponding reconstruction obtained using noiseless data.

The obtained results show that noticeable degradation in the reconstructed MWI images begins to appear at around 10 dB SNR (the point at which the noise level becomes comparable to the modeling error associated with the initial coarse two-layer model.

In the next step, the continuous images are discretized to extract the skull boundaries. To determine the optimal threshold, we used a histogram. Figure 7 shows the histogram for one of the top cross-sections ($z = z_{27}$). For better clarity, we present the estimated real part of the permittivity instead of the contrast. In the layers closest to the antennas (i.e., the top layers), the histograms consistently exhibit three distinct regions: one centered around 46, corresponding to soft tissue; another above 50, corresponding to brain tissue; and a third below 43, associated with the skull. Based on these observations, a threshold value of threshold (TH) = 44 is selected.

After binarizing the image using the threshold derived from the histograms, the external and internal skull boundaries are identified and then used to generate a skull model. Once the skull model is generated, the approximate head model is obtained by inserting the skull in the background model from Fig. 1 (b). The model comprises four distinct domains: (1) skull, (2) brain, (3) skin with fat, and (4) soft tissue occupying the remaining volume. The brain and skull regions were flattened at the depth corresponding to the effective field penetration, as the scattered fields originating from layers below this level were found to be negligible. The obtained phantom is presented in Fig. 8.

https://doi.org/10.1017/S175907872610333X Published online by Cambridge University Press

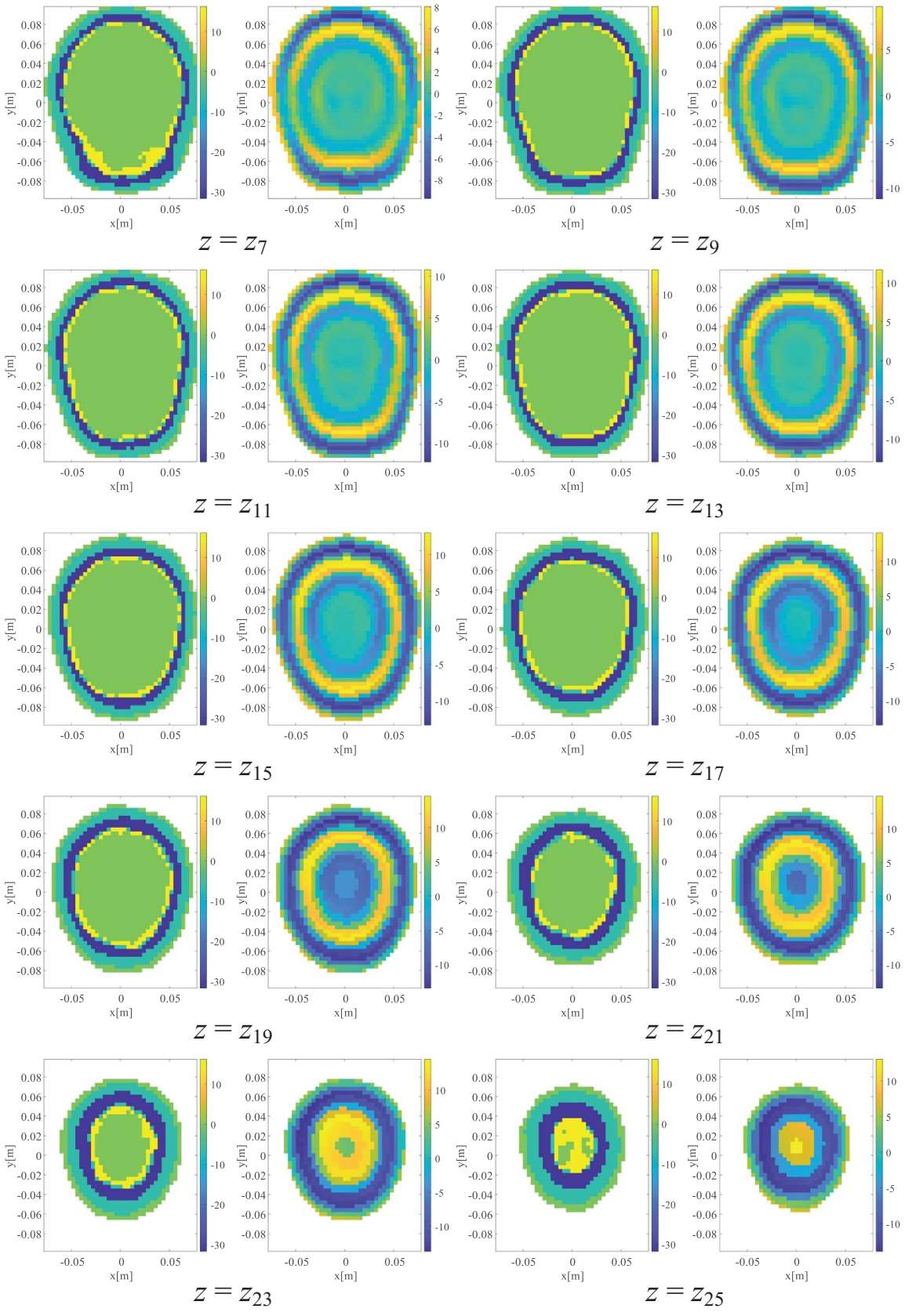


Figure 4. Reconstructed permittivity differences in various horizontal cross-sections (z-cuts), on the right, and corresponding ground truth, on the left.

https://doi.org/10.1017/S175907872610333X Published online by Cambridge University Press

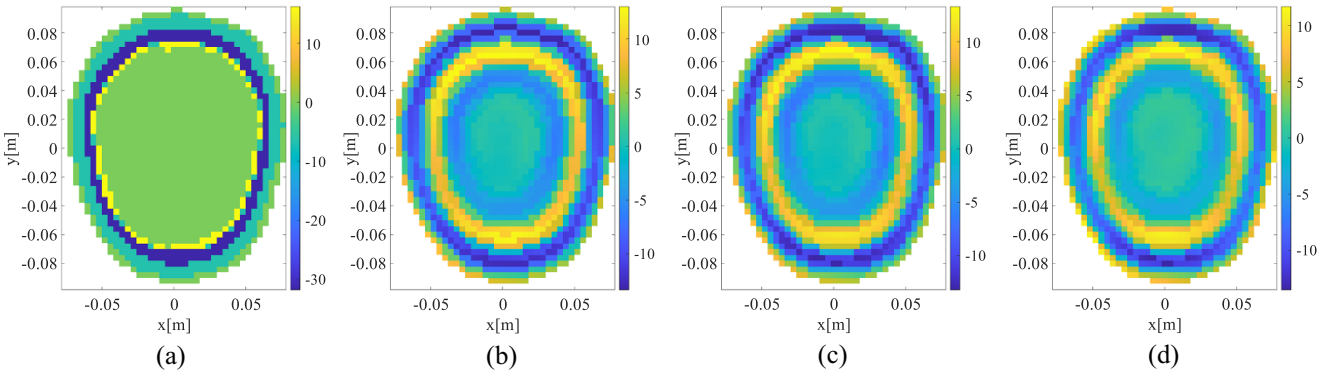


Figure 5. Permittivity differences in the horizontal cross-section $z = z_{15}$: (a) ground truth, and reconstructed values obtained with (b) $L = 3$, $N = 25$, (c) $L = 3$, $N = 30$, and (d) $L = 4$, $N = 30$.

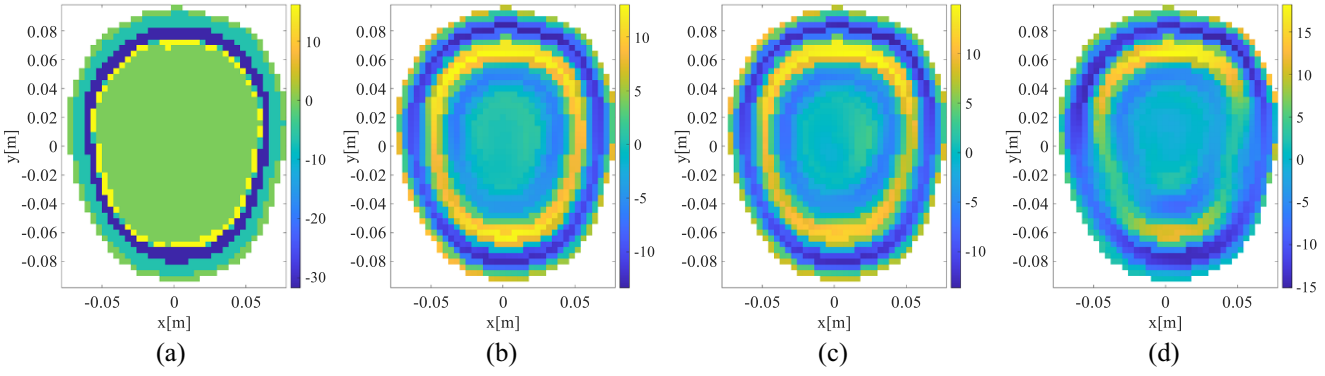


Figure 6. Permittivity differences in the horizontal cross-section $z = z_{15}$: (a) ground truth, and reconstructed values obtained with (b) noiseless data, (c) SNR = 20 dB, and (d) SNR = 10 dB.

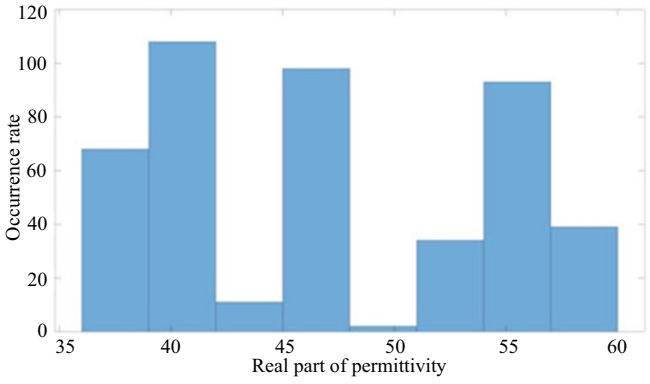


Figure 7. Typical histogram of the estimated real part of the permittivity in top layers ($z = z_{27}$).

DBIM results

In order to complete the patient-specific model, the permittivities of the four domains should be calculated. To that aim, the DBIM procedure described in the "DBIM formulation with known domain boundaries" subsection was employed. The same search space, comprising 34,947 voxels inside the head, was used as in the previous subsection. Once the DBIM was performed and the values of permittivities were obtained, the scattering matrix of the patient-specific model was calculated using WIPL-D Pro. To evaluate the accuracy of the approximation of the original six-domain model by the obtained model, the relative root mean square error (RRMSE) of the scattering parameters, denoted as δ, was computed:

$$\delta = \sqrt{\frac{\sum_{k=1}^{M}\sum_{j=1}^{M}\left|s_{kj} - s_{kj}^{ref}\right|^2}{\sum_{k=1}^{M}\sum_{j=1}^{M}\left|s_{kj}^{ref}\right|^2}} \cdot 100\ \%, \tag{24}$$

where s_{kj} and s_{kj}^{ref} are the scattering parameters calculated for the model obtained from the DBIM and the original model with six tissues (Fig. 1 (a)), respectively.

As the first test of the DBIM, we assumed the boundaries of the six-domain phantom from Fig. 1(a) were precisely known. The initial values of permittivity for all tissues were set to the average value (34.64–j12.68) from [24]. In this case, the DBIM converged to the permittivity actual values from Table 1 after five iterations.

Furthermore, to assess the maximal accuracy that can be obtained from the model with four tissues, two parametric models were created from the original model with six tissues, assuming that intertissue boundaries are known. Namely, the facial bones were removed from the skull, and the true skull boundaries were parameterized using spherical harmonics, up to two different cutting planes. As a result, parametric model 1 (Fig. 9(a)) and parametric model 2 (Fig. 9(b)) were obtained.

For both parametric models and the patient-specific model from Fig. 7, the DBIM converged within 10 iterations (7 iterations for the patient-specific model and 6 iterations for each of the parametric models). Each of the three WIPL-D models had

https://doi.org/10.1017/S175907872610333X Published online by Cambridge University Press

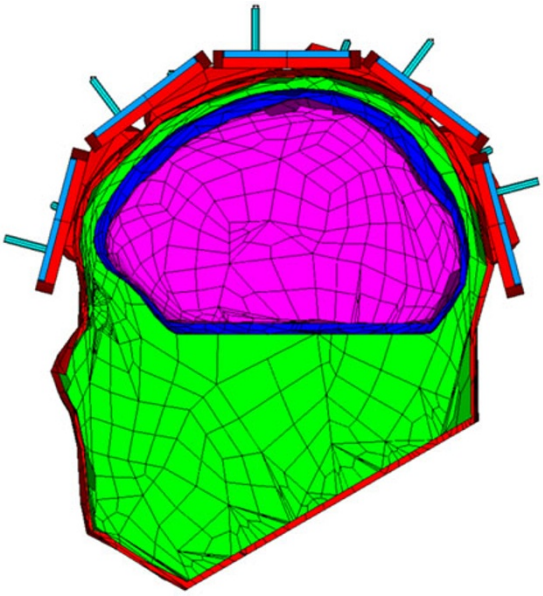


Figure 8. Geometry of the obtained patient-specific model with four tissues.

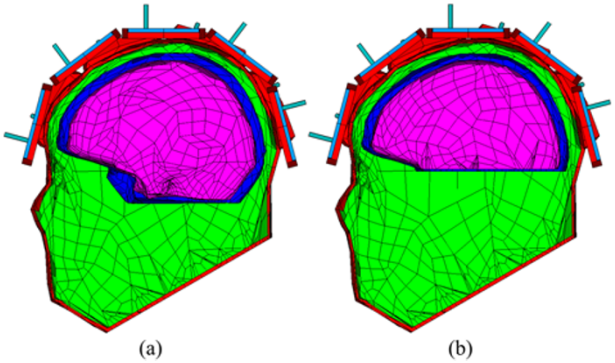


Figure 9. (a) Parametric model 1. (b) Parametric model 2.

Table 2. DBIM results

	Patient-specific model	Parametric model 1	Parametric model 2
Skin and fat permittivity	29.17–j10.17	32.84–j10.35	32.27–j10.55
Soft tissue permittivity	44.49–j12.38	39.30–j16.73	38.92–j15.84
Skull permittivity	24.50–j13.17	17.63–j5.80	14.74–j5.84
Brain permittivity	50.04–j30.86	58.06–j17.61	57.31–j16.96
δ	**4.27%**	**3.54%**	**3.55%**

around 33,000 unknowns, and thus each DBIM iteration lasted for about 50 min. The obtained values of permittivities and RRMSE are presented in Table 2.

When the exact skull boundaries were used for the parameterization, RRMSE values of 3.54% and 3.55% were achieved. On the other hand, for a patient-specific model created from the reconstructed permittivities, an RRMSE of 4.27% was attained.

Table 3. DBIM results for the patient-specific model with AWGN applied to the scattering parameters at different SNR levels

SNR level	SNR = 20 dB	SNR = 15 dB	SNR = 10 dB
Skin and fat permittivity	30.08–j10.76	31.11–j12.62	29.44–j12.92
Soft tissue permittivity	43.30–j13.38	40.76–j13.46	43.33–j10.64
Skull permittivity	23.46–j11.17	22.94–j13.53	33.70–j11.05
Brain permittivity	49.58–j30.49	41.79–j31.87	62.25–j35.34
δ	**4.30%**	**4.57%**	**6.25%**

For comparison, the minimum RRMSE that could be obtained by approximating the original model with the homogenous head phantom was 12.27%. Thus, the patient-specific four-tissue model that used the same a priori information achieved almost three times lower value of error.

For the initial two-layer model used for the generation of the patient-specific model, the RRMSE was 26.3%. Equivalently, the signal-to-modeling-error power ratio improved from about 11 dB for the initial two-layer model to approximately 27.4 dB for the patient-specific model.

Moreover, the robustness of the DBIM with respect to measurement noise was evaluated by incorporating AWGN into the simulated scattering parameters of the original six-domain model. Noise levels corresponding to SNR values of 20, 15, and 10 dB were considered.

To isolate the effect of noise on the DBIM algorithm, independent of its impact on the construction of the four-domain phantom, the tissue geometry obtained under noiseless conditions was employed. The corresponding permittivity estimates and RRMSE values are reported in Table 3. In all cases, the DBIM algorithm converged within 10 iterations.

As shown in Table 3, reconstruction accuracy gradually decreases with decreasing SNR, reflecting the growing influence of noise. For SNR levels of 20 and 15 dB, the estimated permittivity values remain close to those obtained in the noiseless case, with only a moderate increase in RRMSE. Even at an SNR of 10 dB, the DBIM algorithm converges reliably, although deviations in the permittivity of inner tissues (such as the skull and brain) become more pronounced. These findings are consistent with the MWI results presented in Fig. 6, where an SNR of 10 dB relative to the total signal appears to represent a threshold beyond which more significant degradation occurs. Considering that stroke-related signals are more than 50 dB weaker than the total signal, it can be concluded that the examined noise levels are unlikely to significantly impact the primary application of the patient-specific background model.

Conclusion

This work has presented an advanced methodology for constructing patient-specific head models to enhance quantitative MMWI. The proposed framework integrates an anatomically conformal parameterization of the head geometry, obtained through a spherical harmonic approximation of the interpolated surface points. This approach ensures a geometrically consistent representation of the region of interest, particularly in the upper cranial portion,

https://doi.org/10.1017/S175907872610333X Published online by Cambridge University Press

which is relevant in microwave measurements, and it provides a practical pathway for building individualized models directly from measured data.

The proposed method was assessed numerically, building upon a realistic six-tissue head phantom derived from the NEVA female anatomical model. The simulations were conducted in the WIPL-D Pro environment using a 21-antenna helmet array operating at 1 GHz. A linearized reconstruction was first applied to estimate the real part of the permittivity contrast, followed by histogram-based segmentation to delineate the skull boundaries and define four distinct tissue domains. The permittivity values of these tissues were then quantitatively estimated using the DBIM. The resulting patient-specific four-tissue model achieved a RRMSE of 4.27%, closely matching the 3.54% obtained using exact skull boundaries and significantly outperforming the homogeneous head approximation (12.27% RRMSE).

These results demonstrate that the proposed modeling strategy substantially improves the accuracy of DBIM, while maintaining computational efficiency. The capability to generate reliable individualized background models directly from microwave data represents a significant step toward enhancing the initialization and convergence of quantitative inverse scattering algorithms, thus advancing MMWI toward practical clinical implementation.

Acknowledgement. This work was supported in part by the Ministry of Science, Technological Development and Innovations of the Republic of Serbia, under Contract 451-03- 137/2025-03/200103.

Competing interests. The authors report no conflict of interest.

References

1. **Chandra R, Zhou H, Balasingham I and Narayanan RM** (2015) On the opportunities and challenges in microwave medical sensing and imaging. *IEEE Transactions on Biomedical Engineering* **62**(7), 1667–1682. https://doi.org/10.1109/TBME.2015.2432137
2. **Crocco L, Karanasiou I, James M and Conceição R** (2018) *Emerging Electromagnetic Technologies for Brain Diseases Diagnostics, Monitoring and Therapy*. Cham, Switzerland: Springer.
3. **Hopfer M, Planas R, Hamidipour A, Henriksson T and Semenov S** (2017) Electromagnetic tomography for detection, differentiation, and monitoring of brain stroke: A virtual data and human head phantom study. *IEEE Antennas and Propagation Magazine* **59**(5), 86–97. https://doi.org/10.1109/MAP.2017.2732225
4. **Pastorino M** (2010) *Microwave Imaging*. Hoboken, New Jersey, USA: John Wiley & Sons.
5. **Persson M et al** (2014) Microwave-based stroke diagnosis making global prehospital thrombolytic treatment possible. *IEEE Transactions on Biomedical Engineering* **61**(11), 2806–2817. https://doi.org/10.1109/TBME.2014.2330554
6. **Gong Z, Chen Y, Ding Y and Zhang H** (2024) Perspective: Microwave medical imaging using space-time-frequency a priori knowledge for health monitoring. *IEEE Journal of Electromagnetics, RF and Microwaves in Medicine and Biology* **8**(1), 2–14. https://doi.org/10.1109/JERM.2023.3337660
7. **Mousavi SSS and Majedi MS** (2024) A modified microwave imaging method for brain stroke detection. *IEEE Transactions on Antennas and Propagation* **72**(1), 890–900. https://doi.org/10.1109/TAP.2023.3330294
8. **Bozza G, Estatico C, Pastorino M and Randazzo A** (2006) An inexact Newton method for microwave reconstruction of strong scatterers. *IEEE Antennas and Wireless Propagation Letters* **5**, 61–64. https://doi.org/10.1109/LAWP.2006.870360
9. **Bozza G and Pastorino M** (2009) An inexact newton-based approach to microwave imaging within the contrast source formulation. *IEEE Transactions on Antennas and Propagation* **57**(4), 1122–1132. https://doi.org/10.1109/TAP.2009.2015820
10. **Guo L, Nguyen-Trong N, AI-Saffar A, Stancombe A, Bialkowski K and Abbosh A** (2022) Calibrated frequency-division distorted born iterative tomography for real-life head imaging. *IEEE Transactions on Medical Imaging* **41**(5), 1087–1103. https://doi.org/10.1109/TMI.2021.3132000
11. **Guo L, Khosravi-Farsani M, Stancombe A, Bialkowski K and Abbosh A** (2022) Adaptive clustering distorted born iterative method for microwave brain tomography with stroke detection and classification. *IEEE Transactions on Biomedical Engineering* **69**(4), 1512–1523. https://doi.org/10.1109/TBME.2021.3122113
12. **Karadima O, Lu P, Sotiriou I and Kosmas P** (2022) Experimental validation of the DBIM-TwIST algorithm for brain stroke detection and differentiation using a multi-layered anatomically complex head phantom. *IEEE Open Journal of Antennas and Propagation* **3**, 274–286. https://doi.org/10.1109/OJAP.2022.3150100
13. **Suzuki Y and Kidera S** (2021) Resolution enhanced distorted Born iterative method using ROI limiting scheme for microwave breast imaging. *IEEE Journal of Electromagnetics, RF and Microwaves in Medicine and Biology* **5**(4), 379–385. https://doi.org/10.1109/JERM.2021.3121962
14. **Islam MS, Islam MA and Kiourti A** (2026) Improved microwave imaging with the extended born iterative method. *IEEE Transactions on Antennas and Propagation* **74**(1), 848–858. https://doi.org/10.1109/TAP.2025.3620041
15. **Ninković D, Kovačević A, Kolundžija B, Scapaticci R, Crocco L and Nikolić Stevanović M** (2025) Permittivity estimation for patient-specific head model via DBIM. In *2025 19th European Conference on Antennas and Propagation (EuCAP)*, Stockholm, Sweden, pp.1–5. https://doi.org/10.23919/EuCAP63536.2025.10999522
16. **Ninković D, Kovačević A, Kolundžija B, Crocco L and Stevanović MN** (2026) Patient-specific background model estimation for effective brain stroke microwave imaging. *IEEE Transactions on Medical Imaging* https://doi.org/10.1109/TMI.2026.3660568.
17. **Nikolova N** (2017) *Introduction to Microwave Imaging*. Cambridge: Cambridge University Press.
18. **Nikolić Stevanović M and Đorđević A** (2022) Simple derivation of transfer functions in bistatic scattering model. *IEEE Transactions on Antennas and Propagation* **70**(10), 9867–9870. https://doi.org/10.1109/TAP.2022.3177456
19. **NEVA EM** [Online], Available at https://www.nevaelectromagnetics.com/.
20. **WIPL-D Pro v20** (2024) 3D Electromagnetic Solver. WIPL-D d.o.o, Belgrade, Serbia. http://www.wipl-d.com
21. **Singh T, Ninkovic BM, Tasic MS, Stevanovic MN and Kolundzija BM** (2023) 3-D EM modeling of medical microwave imaging scenarios with controllable accuracy. *IEEE Transactions on Antennas and Propagation* **71**(2), 1640–1653. https://doi.org/10.1109/TAP.2022.3209244
22. **Ninković D, Ruiz ÁY, Nikolaou S, Crocco L, Kolundžija B and Stevanović MN** (2024) Polynomial basis functions for qualitative head tissue segmentation via linearized microwave imaging. In*2024 18th European Conference on Antennas and Propagation (EuCAP)*, Glasgow, United Kingdom, pp. 1–5, https://doi.org/10.23919/EuCAP60739.2024.10501162
23. **Scapaticci R, Di Donato L, Catapano I and Crocco L** (2012). A feasibility study on microwave imaging for brain stroke monitoring. *Progress In Electromagnetics Research B* **40**, 305–324. https://doi.org/10.2528/PIERB12022006
24. **Singh T, Ninkovic B, Tasic M, Stevanovic MN and Kolundzija B** (2022) New method for calculation of average electric properties of reference head phantom in microwave imaging," *2022 16th European Conference on Antennas and Propagation (EuCAP)*, Madrid, Spain, pp. 1–5. https://doi.org/10.23919/EuCAP53622.2022.9769058.



Darko Ninković was born in Belgrade, Serbia, in 1995. He received the BSc and MSc degrees in electrical engineering from the School of Electrical Engineering, University of Belgrade, in 2018 and 2019, respectively, where he is currently pursuing the PhD degree. His current research interests include microwave imaging, optimization algorithms and machine learning applied to the electromagnetic analysis, electromagnetic compatibility, and numerical electromagnetic analysis.



Anja Kovačević was born in Belgrade, Serbia, in 1999. She received the BSc and MSc degrees in electrical engineering from the School of Electrical Engineering, University of Belgrade, in 2022 and 2023, respectively, where she is currently pursuing the PhD degree. In 2022, she joined the School of Electrical Engineering, University of Belgrade, as a teaching associate and currently is a teaching assistant at the same school. Her current research interests include microwave imaging, microwave passive circuits and electromagnetic compatibility. She was a recipient of IEEE MTT-S Undergraduate Scholarships – 2023 Cycle 1 Award.



Branko Kolundžija was born in Zenica, former Yugoslavia, in 1958. He received the BSc, MSc, and DSc degrees from the University of Belgrade, Belgrade, Serbia, in 1981, 1986, and 1990, respectively. He joined the School of Electrical Engineering, University of Belgrade, in 1981, as an assistant-trainee, in 1986 as an assistant, in 1991 as an assistant professor, in 1998 as an associate professor and in 2003 as a full professor, teaching electromagnetics, antennas and propagation of radio waves, software tools for designing antennas, and modeling and simulation of electromagnetic fields. He is the author/coauthor of two monographs, five monograph chapters, three monographs accompanied by software packages, one textbook, more than 60 journal articles, and more than 200 articles at international conferences, in the areas of numerical and theoretical electromagnetics, antennas, microwave technique, electromagnetic compatibility, applied mathematics, and artificial intelligence. He is the main architect of the WIPL-D software suite.



Rosa Scapaticci received her master's degree with honors in Biomedical Engineering from the University of Naples "Federico II" in 2010 and her PhD in Information Engineering from the "Mediterranea" University of Reggio Calabria in 2014. She is currently a senior researcher at the Institute for Electromagnetic Sensing of the Environment of the Italian National Research Council in Naples. Her research focuses on electromagnetic scattering and imaging techniques for noninvasive diagnostics, with particular emphasis on developing innovative microwave imaging approaches for biomedical applications. She received the Best Student Member Paper Award from the IEEE Antennas and Propagation Society in 2013, and the Barzilai and Latmiral Awards from the Italian Society of Electromagnetics in 2014 and 2018, respectively. In 2021, she obtained the National Scientific Qualification as Associate Professor in electromagnetic fields. From March 2022 to April 2026, she served as Associate Editor for *IEEE Transactions on Medical Imaging*.



Lorenzo Crocco is Research Director at the Institute for Electromagnetic Sensing of the Environment, National Research Council of Italy (IREA-CNR). His research focuses on electromagnetic scattering methods and applications, with particular emphasis on noninvasive diagnostics and therapeutic uses of electromagnetic fields. He has authored over 120 papers and edited two books. Since 2021, he has been listed in the World's Top 2% Scientists database. He serves on the Scientific Board of the Italian Electromagnetic Society and the CNR Engineering Department Scientific Board. Since 2014, he has been a Board Member of the European School of Antennas (ESoA). Since 2024, he has represented Italy, San Marino, and Vatican City in the Delegate Assembly of the European Association on Antennas and Propagation (EurAAP). Within EurAAP, he also founded the Working Group on Electromagnetic Technologies for Life Science Applications (ELSA). Lorenzo Crocco is an IEEE Senior Member and URSI Senior Member.



Marija Nikolić Stevanović received the BSc, MSc, and PhD degrees in electrical engineering from the University of Belgrade, Serbia, in 2000, 2003, and 2007, respectively, and an additional PhD degree from Washington University in St. Louis, USA, in 2011. In 2011, she joined the School of Electrical Engineering at the University of Belgrade as a teaching assistant and was promoted as Full Professor in 2022. Her research interests include inverse scattering, microwave imaging, numerical electromagnetics, and antenna design. In recent years, her work has focused particularly on microwave medical imaging. She has served as the Serbian representative on the Management Committees of COST Actions dedicated to medical applications of electromagnetic fields, including MiMed (microwave imaging) and MyWAVE (therapeutic applications of electromagnetic waves). She also served as Vice-Dean for Research at the School of Electrical Engineering during 2024–2025.

https://doi.org/10.1017/S175907872610333X Published online by Cambridge University Press